Pre-print submitted version

Hybrid vapor-solution sequentially deposited mixed-halide perovskite solar cells

Wiria Soltanpoor[1,2], Chris Dreessen[3], Mehmet Cem Sahiner[1,4], Isidora Susic[3], Amir Zarean Afshord[1,2], Vladimir S. Chirvony[3,5], Pablo P. Boix[5,] , Gorkem Gunbas[1,2,6,7,], Selcuk Yerci[1,2,4,*], Henk J. Bolink[3,*]*

[1]The Center for Solar Energy Research and Applications (GUNAM), Middle East Technical University, Ankara, 06800, Turkey

[2]Department of Micro and Nanotechnology, Middle East Technical University, Ankara, 06800, Turkey

[3]Instituto de Ciencia Molecular, Universidad de Valencia, C/Catedrático J. Beltrán 2, 46980 Paterna, Spain

[4]Department of Electrical and Electronics Engineering, Middle East Technical University, Ankara, 06800, Turkey

[5]Instituto de Ciencia de Materiales, Universidad de Valencia, C/Catedrático J. Beltrán, 2, 46980 Paterna, Spain

[6]Department of Polymer Science and Technology, Middle East Technical University, Ankara, 06800, Turkey

[7]Department of Chemistry, Middle East Technical University, Ankara, 06800, Turkey

KEYWORDS. Perovskite, solar cells, vapor phase deposition, interdiffusion, halide assisted crystallization.

ABSTRACT

The recent sky-rocketing performance of perovskite solar cells has triggered a strong interest in further upgrading the fabrication techniques to meet the scalability requirements of the photovoltaic industry. The integration of vapor-deposition into the solution process in a sequential fashion can boost the uniformity and reproducibility of the perovskite solar cells. Besides, mixed-halide perovskites have exhibited outstanding crystallinity as well as higher stability compared with iodide-only perovskite. An extensive study was carried out to identify a reproducible process leading to highly crystalline perovskite films that when integrated into solar cells exhibited high power conversion efficiency (max. 19.8%). This was achieved by optimizing the deposition rate of the PbI_2 layer as well as by inserting small amounts of methylammonium (MA) bromide and chloride salts to the primary MAI salt in the solution-based conversion step.

The optimum MABr/MAI molar ratio leading to the most efficient and stable solar cells was found to be 0.4. Stabilities were in excess of 90 hours for p-i-n type solar cells. This reproducible approach towards the fabrication of triple halide perovskites using a hybrid vapor-solution method is a promising method towards scalable production techniques.

1. Introduction

The unprecedented evolution of halide perovskites optoelectronics, achieving photovoltaic efficiencies beyond 25.2% in less than 11 years, stems from their high absorption coefficients, long charge carrier diffusion lengths and adjustable bandgaps[1,2,3,4,5,6]. In contrast with conventional methylammonium lead iodide ($CH_3NH_3PbI_3$ or MAPI), partial replacement of methylammonium (MA) with formamidinium (FA) and Cesium (Cs), has exhibited enhanced thermal, moisture and mechanical stability of the perovskite layer[7,8,9,10]. Also, including fractional bromide (Br^-) instead of iodide (I^-), has proven to boost the crystal formation and the phase stability of the perovskite[9,11]. A myriad of fabrication techniques for making potentially low cost yet high-quality perovskites have been developed which mainly include solution-based and/or evaporation techniques. The solution process is popular due to the ease of stoichiometric control and its low-cost nature. Thus, most of the reported record efficiencies have been achieved using wet chemical processes. In this category, in single-step perovskite fabrication method, where all the precursors are in the same solution, the crystallization of the perovskite film is controlled using anti-solvent engineering or other post-treatments like heat or vacuum quenching[12] . However, for large area production an alternative coating method referred to as the

sequential deposition method, in which each step involves the use of a solution with only one type of the perovskite precursor salts, has been shown to result in more uniform pin-hole free perovskite layers[13,14,15] . Despite the simplicity of the solution process, it often lacks reproducibility and it is not trivial to apply on large-area solar cells[16] . On the other hand, techniques such as co-evaporation render high uniformity and thickness control of the perovskite layer with nominal efficiencies above 20%[17,18] . The all evaporated sequential method also proved as a promising method in achieving highly crystalline perovskite films with 17.6% efficiency[19] . In principle, evaporation-based methods are appealing since industrial scale devices can be realized due to their high reproducibility and uniformity. However, it is not straightforward to construct multi-halide or multi-cation perovskites with stoichiometric precision. As a result, combining evaporation and solution-based processing in a sequential fashion referred to, from now on, as hybrid vapor-solution technique is a promising alternative taking advantage of the particular benefits of both vapor phase deposition and solution processing such as uniformity, processing time, and low capital investment[20] . In the hybrid vapor-solution method, first, a layer of lead halide (PbX_2 with X = I, Cl) is vacuum deposited and then the organic component is introduced by exposing the film to an alcohol solution containing MA- or FA-halide, either by spin-coating or via immersion[14,20,21,22,23] . Vapor deposition of the inorganic PbX_2 leads to a uniform layer on the substrate. In addition, since the formation of the perovskite is accompanied by volume expansion of the initial PbX_2 layer, the final structure is a continuous pin-hole-free perovskite film. This makes the method particularly interesting for roll-to-roll production procedures such as slot-die and spray coating[24,25] . Recently, Rafizadeh *et. al.* used a hybrid vapor-solution method to fabricate planar MAPI-based devices with 18.9% efficiency in the n-i-p structure[26] . In that work, TiO_2 was used as the

electron transport layer for the evaporated PbI_2 layer. On that surface, a porous PbI_2 was formed which facilitates its transformation into perovskite during the second (solution-based) step. However, using TiO_2 in direct contact with perovskite often results in hysteresis[26,27,28,29] . Applying organic inter/sublayers has widely been shown to mitigate the hysteresis[17,30,31,32] . Hence, it is of interest to perform sequential deposition on organic charge transport layers. On these less polar surfaces, however, the vapor phase deposited PbI_2 film is a dense (non-porous) film which is harder to convert into a perovskite film, in particular for thick films, as was also described previously[21] .

Here we show that by employing diffusive ions such as Br^- or Cl^- in the solution step, the conversion of the PbI_2 layer into perovskite is greatly facilitated. This method leads to reproducible perovskite films and allows for the preparation of a wide range of mixed halide compositions. The latter is of interest as these mixed halide perovskites possess larger charge carrier mobilities and longer diffusion lengths which can suppress the hysteresis[6] . Moreover, it was shown by Sun *et. al.* that the addition of Br^- and Cl^- enhances the crystallinity and photoluminescence quantum yield (PLQY) of the perovskite film[33] .

Hence, we analyze the main crystallization and perovskite formation processes in each step of the sequential hybrid vapor-solution fabrication method. In the first step, the inclusion of Br^-, Cl^- and their combination in the MA-halide solution, was thoroughly investigated both on the film properties and when integrated into solar cells. Using the optimum conversion mixture, we then studied the effect of the PbI_2 deposition rate on the inorganic layer roughness, on the crystallization of the perovskite layer, and on the device performance. This allowed us to optimize the solar cells further, reaching power conversion efficiencies as high as 19.8% with open circuit voltages (V_{OC}) above 1.1 V and fill factors above 82% with no hysteresis. Such

performance enhancement was shown to stem from the improved crystallinity of mixed halide perovskites and reduced nonradiative recombination within the structure of the perovskite solar cell. While Cl^- was effective to transform the initial PbI_2 layer into perovskite, the addition of Br^- was found to be essential for sustaining the operational stability.

2. Experimental Section

Pre-patterned ITO coated glass substrates were purchased from Naranjo substrates. Molybdenum oxide (MoO_3), bathocuproine (BCP) and Methylammonium chloride (MACl) were obtained from Lumtec, N4,N4,N4″,N4″-tetra([1,1′-biphenyl]-4-yl)-[1,1′:4′,1″-terphenyl]-4,4″-diamine (TaTm) was provided by Novaled GmbH. Fullerene (C_{60}) and anhydrous isopropanol (IPA) were obtained from Sigma-Aldrich. Methylammonium iodide (MAI) and Methylammonium bromide (MABr) were bought from GreatCell Solar. PbI_2 was purchased from Tokyo Chemical Industries (TCI).

The ITO-coated substrates were sonicated for 10 minutes successively in soap, deionized water, and isopropanol, followed by UV-ozone treatment for 15 minutes. Then, the samples were transferred into a vacuum chamber integrated into a N_2-glovebox. A 6 nm-thick MoO_x was thermally evaporated at a base pressure of 2×10^{-7} Torr onto the substrates followed by an annealing step at 100 °C for 10 minutes. Later, 10-nm thick TaTm was thermally deposited under a vacuum of 5×10^{-6} Torr, followed by 250 nm-thick PbI_2 at rates of 2, 2.5 and 3.5 Å/s for the rate study and 2.5 Å/s for the rest of the paper. The deposition rate was monitored using quartz crystal microbalance (QCM). Later, the MA-halide solution was spin-cast at 2100 rpm for 30 seconds on top of ITO/MoO_x/TaTm/PbI_2-coated substrates, which was followed by an annealing step at 100 °C for 45 minutes to form the perovskite layer. The substrates were washed twice by IPA and dried on a hot plate at 100 °C. Unless otherwise stated, the MA-halide solution

consisted of MAI (35mg), MABr (10 mg) and MACl (5 mg) per 1 ml of anhydrous IPA. The perovskite coated substrates were transferred into a vacuum chamber to deposit C_{60} and BCP (25 and 7nm, respectively) as electron transport layers at a base pressure of 5×10^{-6}Torr. Finally, a 100 nm-thick Ag was deposited by thermal evaporation at a pressure of 2×10^{-7} Torr to form the electrode.

The external quantum efficiency (EQE) was measured using a white halogen lamp combined with band-pass filters. The solar spectrum was corrected according to a silicon reference cell, previously calibrated (MiniSun simulator by ECN, Holland). The J–V characteristics were measured using a solar simulator by Abet Technologies, model 10500, with an AM1.5G xenon lamp as the light source and Keithley 2400 as the electronic sweeping unit. A shadow mask with an aperture of 0.06 cm^2 was used to define the active area of the cells. The X-Ray diffractometry for Figures S1a and 1a were collected using an Empyrean PANanalytical powder diffractometer with Cu Kα1 radiation. The XRD for Figure 1i and Figure S4 were obtained Rigaku MiniFlex with Cu Kα1 radiation. The optical properties were measured using fiber optics-based Avantes Avaspec2048 Spectrometer. AFM topography was measured using Veeco MultiMode V. The morphological and cross-sectional SEM images were obtained by Hitachi S-4800 and Zeiss EVO HD15 electron microscopes at an accelerating voltage of 20 kV. Before running the stability measurements, the solar cells were encapsulated laminating a foil provided by Tesa GmbH. The device stability measurement was carried out via a system by Candlelight, recording J–V parameters every 15 minutes under white LED source with irradiance equivalent to 1 Sun. The system was water-cooled to keep the devices at 300 K throughout the measurement. Photoluminescence (PL) spectra were measured by pumping the sample with a 200 fs pulsed Ti:sapphire laser (Coherent Mira 900D) at a repetition rate of 76 MHz doubled to 405 nm with a

BBO crystal. The backscattered PL signal was dispersed by a double 0.3-m focal length grating spectrograph/spectrometer (1200 g/mm) and detected by a CCD camera.

3. Results and Discussion

3.1 The effect of Br^- and Cl^- and their combination

The initial PbI_2 layer can be deposited either by solution or evaporation during the two-step sequential method. Evaporation enables effective control over the thickness, crystallinity, and morphology of a highly pure PbI_2 layer without residual solvents. The quality of the final perovskite layer depends predominantly on the properties of the initial PbI_2 film[14] . After introducing the organic MA-halide solution, the reaction initially takes place at PbI_2 crystal defects and follows the Ostwald's step rule to reduce Gibbs free energy engendering perovskite[34] . The reaction between PbI_2 and MA-halide components starts by forming a capping layer of perovskite on top followed by a dissolution-recrystallization process and a series of PbI_2 grain migration within the film to form perovskite[35] . The crystallization of the capping layer at the surface is rapid and can impede the effective interdiffusion of the organic precursors into the integral bulk of the PbI_2 layer. A thickness of 250 nm was chosen as the standard for the sublimed bottom layer of PbI_2 throughout this study. The perovskite layer was subsequently formed by spin-casting an IPA solution of MAI (35 mg/ml). The perovskite layer was rough with grains in the form of humps with heterogeneous sizes (shown by SEM image in Figure 1a) which might be due to relatively high strain between the crystallites[36] . The conversion of the PbI_2 layer into perovskite after applying the MAI solution is incomplete leaving behind an unreacted 50 nm thick PbI_2 layer between the perovskite layer and the bottom substrate as evidenced by the SEM image in Figure 1b. The unreacted PbI_2 in the final perovskite resulted in an intense PbI_2 (100)

diffraction at 12.7˚ according to Figure 1i. To resolve this incomplete conversion and improve the mass transfer of the organic compounds during the sequential method, many routes have been proposed. These range from adding ammonium acid iodide (AAI) derivatives to PbI_2 precursor[37] , treating PbI_2 with chlorobenzene[38] , introducing cyclohexane to MA-iodide solution to lower the solution polarity[39] , and incorporating Cl^- during a multi-cycle dropping technique[40] . Among all, during the sequential approach, the inclusion of small halide ions such as Cl^- and Br^- has been shown to improve the mass transfer of MA compounds into the solution deposited PbI_2 layer[33,41] . However, whether this observation is also valid for vapor deposited PbI_2 films and how the evaporation rate of the PbI_2 affects the perovskite film quality, was not investigated. This is important as vapor phase deposition allows for thickness control, precise positioning (via shadow masks) and leads to uniform and smooth films. However, such PbI_2 films, are denser than solution processed PbI_2 films, and therefore, are more difficult to convert to the perovskite phase. This is especially difficult when they are deposited on top of organic semiconductor films. Therefore, we introduce MACl, MABr, and a mixture of both to facilitate the diffusion of the organic solutes through the densely packed PbI_2 grains to effectively convert them into the perovskite layer. To identify the final perovskite film, we use a nomenclature that considers the halides present in the MA-halide solution. When the solution is composed of MAI only, the resultant perovskite is denoted as MAPI. If MACl (5 mg/ml) or MABr (10 mg/ml) is added, the perovskite is named MAPI-Cl or MAPI-Br, accordingly. When both MACl (5 mg) and MABr (10 mg) are added, the perovskite is denoted as MAPI-BrCl. The corresponding molar values of the MA-halides are given in Table S1.

When MACl was added to the MA-halide solution, a more complete conversion of the PbI_2 film was obtained as can be observed from the less intense PbI_2 (100) X-ray diffraction in Figure

1i. Besides, as shown in Figure 1d, the thickness of the unreacted PbI_2 layer was reduced to ≈20 nm (i.e. much thinner compared with MAPI). The grains are more homogenous having a more preferential orientation with respect to MAPI, as shown in Figure 1c-d. This is plausibly due to the inclusion of MACl, which can enhance the perovskite crystallization[41] . Moreover, Cl^- has a higher diffusivity than I^- [42], So it improved the impregnation of MA-halide components into the compact PbI_2 layer in the case of MAPI-Cl. The absorbance is strong with its edge blue-shifted from λ=780 nm to λ=750 nm as shown in Figure 1j.

If MABr (instead of MACl) was added into the MA-halide solution, the transformation of the PbI_2 layer into perovskite was enhanced, which is revealed by the suppressed PbI_2 (100) diffraction in MAPI-Br diffractogram (Figure 1i). This is further proven by the cross-sectional SEM image in Figure 1f where no residual interfacial PbI_2 layer is traceable. According to the surface SEM image in Figure 1e, the crystallites are relatively small but uniform in the case of MAPI-Br. The enhanced conversion of the PbI_2 layer into perovskite as compared to MAPI and MAPI-Cl is likely due to the more diffusive nature of Br^- than I^- [42] and stronger complexation of Pb^{2+} with Br^- than I^- [43]. Besides, the disparity between the ionic sizes of Br^- and I^- is much smaller than that of Cl^-/I^- making the intercalation of Br^- in the perovskite structure more viable than Cl^- [44]. The absorption edge in the case of MAPI-Br was at λ=750 nm similar to MAPI-Cl, as demonstrated in Figure 1j.

When both MABr and MACl were added to the MA-halide solution, the highest conversion of the PbI_2 layer into perovskite was achieved indicated by the smallest PbI_2 (100) diffraction intensity in MAPI-BrCl (Figure 1i). The grains appeared large, uniform, compact and perpendicularly oriented in MAPI-BrCl as shown in Figure 1g-h. Also, the elimination of the unreacted PbI_2 layer at the bottom of the perovskite layer shows that the concurrent inclusion of

Br^- and Cl^- in the MA-halide solution significantly improved the crystallization of perovskite. The absorbance of MAPI-BrCl surpassed the other types of perovskite that were formed with only one or two halides (Figure 1j).

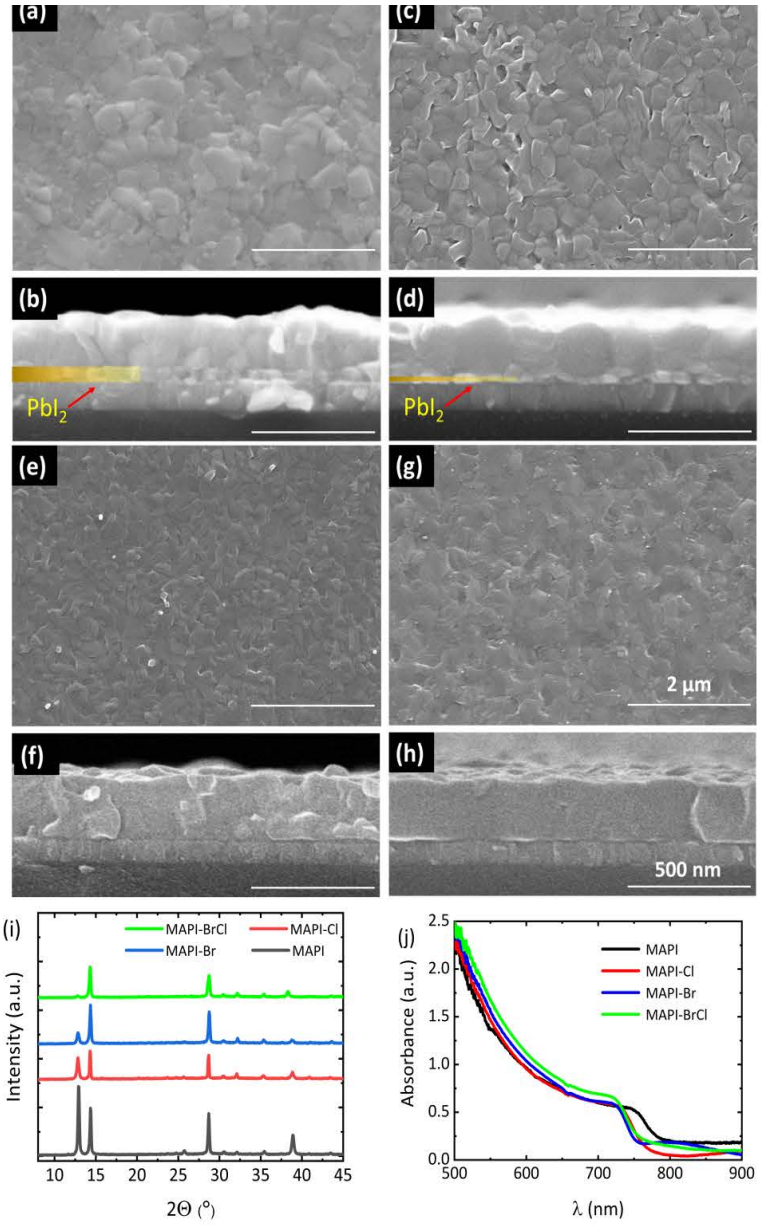

Figure 1. SEM surface and cross-sectional images for a, b) MAPI, the green lines denote the borders of an unreacted PbI_2 layer, c, d) MAPI-Cl, e, f) MAPI-Br, and g, h) MAPI-BrCl, i) XRD

patterns, j) Absorbance spectra for the perovskite layers with single, double and triple halides in the MA-halide solution.

The effect of halide mixing on the performance of the devices was studied in perovskite solar cells fabricated in the p-i-n configuration shown in Figure 2a. In this structure, the perovskite layer is sandwiched between N4,N4,N4′,N4′-tetra([1,1′-biphenyl]-4-yl)-[1,1′:4′,1′-terphenyl]-4,4′-diamine (TaTm)/ molybdenum oxide (MoO_x) as hole transport layer (HTL) and C_{60}/ bathocuproine (BCP) as electron transport layer (ETL). All the transport layers were vacuum deposited as detailed in the Experimental Section. The corresponding EQE spectra, J–V curves, and the extracted performance parameters are presented in Figure 2c-d and Table 1. The device from MAPI suffered from a low FF (53.8%) and minimal charge collection in the short wavelength region of the spectrum (J_{SC} of 17.5 mA/cm^2). These results suggest that the thickness of the unreacted PbI_2 layer at the light incident interface is excessive and acts as a charge collection barrier. In the case of MAPI-Cl, the charge collection was significantly enhanced throughout the whole visible spectrum in contrast with MAPI, which is attributed to the enhanced crystallization of perovskite due to MACl. Also, there is a remarkable improvement in J_{SC} (21.3 mA/cm^2), V_{OC} (1146.3 mV), FF (77.3%) and PCE (18.9%) according to J–V curves in Figure 2d. These results show the beneficial role of MACl inclusion in the effective reaction between PbI_2 and MA-halide solutes. The addition of MABr to MAI solution (referred to as MAPI-Br) also exhibited enhanced EQE and J–V characteristics in contrast with MAPI. According to Figure 2c, the EQE exceeded 85% demonstrating a superior J_{SC} of 22.1 mA/cm^2. Nevertheless, the V_{OC} in the case of MAPI-Br is lower than all the other samples. To explain this, we performed photoluminescence measurements of the prepared perovskite layers with

spectra given in Figure S9. The luminescence curve of MAPI-Br is composed of two peaks at λ=745 nm and λ=781 nm indicating phase segregation. The secondary peak at λ=781 nm is suppressed effectively when both MABr and MACl were added to the MA-halide solution according to Figure S9d. MACl has been reported also by another group to suppress phase segregation in triple-cation perovskites while the current study was under review[45].This can be one of the main reasons that the highest FF (79.6%) and PCE (19.1%) were achieved in the case of MAPI-BrCl in Figure 2c-d. The cross-sectional SEM image (Figure 2b) of MAPI-BrCl solar cell, shows very large grains, spanning the complete distance from hole to electron extracting layer. Nevertheless, the highest V_{OC} (1146.3 mV) was achieved with MAPI-Cl. This is ascribed to the wider phase PbI_2 regions on the surface of MAPI-Cl and a thin unreacted PbI_2 layer between the perovskite and the substrate[46] which is at the expense of J_{SC} loss as compared to MAPI-BrCl. The same holds for the relatively high V_{OC} (1107.1 mV) with thicker PbI_2 in the case of MAPI which, in this case, leads to a dramatic loss in J_{SC} (17.5 mA/cm^2) and FF (53.8%). The highest perovskite quality and efficiency in the case of MAPI-BrCl demonstrate that the simultaneous utilization of MACl and MABr as recrystallizing agents promotes the hybrid vapor-solution sequential method to fabricate perpendicularly oriented grains of perovskite with the best performance.

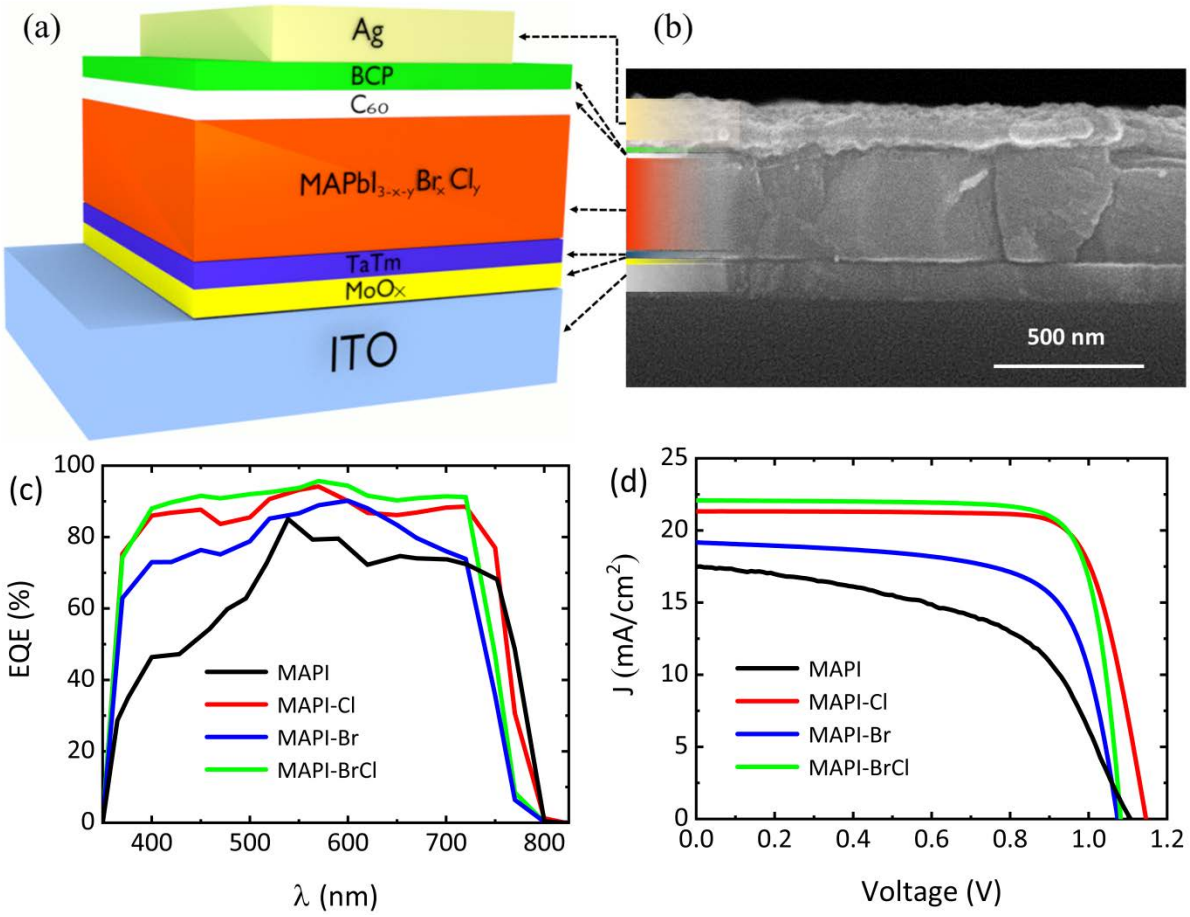

Figure 2. a) Device structure used for perovskite solar cells and b) a cross-sectional SEM image of a full device using MAPI-BrCl as the absorber layer, c) External quantum efficiency, and d) J–V curves for the perovskite solar cells with single, double and triple halides in the MA-halide solution.

Table 1. The extracted performance parameters from J–V curves of the perovskite solar cells with single, double and triple halides in the MA-halide solution which correspond to figure 2d.

Sample	V_{OC} (mV)	J_{SC} (mA/cm^2)	FF (%)	PCE (%)
MAPI	1107.1	17.5	53.8	10.4

MAPI-Cl	1146.3	21.3	77.3	18.9
MAPI-Br	1074.0	19.3	68.7	14.2
MAPI-BrCl	1081.9	22.1	79.6	19.1

3.2 PbI_2 layer and optimal MABr:MAI ratio in MAPI-BrCl

In the first section of this manuscript, we have described the effect of the conversion solution, in particular, the effect that different halide salts have on film formation. In that section, we used one fixed PbI_2 deposition rate. Here, we evaluate how the deposition rate of lead halide can affect the crystallization and the optoelectronic performance of the final perovskite film. We observed that the sublimation rate of PbI_2 is correlated with the reproducibility of the final MAPI-BrCl solar cell. Therefore, we carried out a systematic study on the PbI_2 sublimation rate changing it between 2.0, 2.5 and 3.5 Å/s. The crystallinity and morphology of the PbI_2 layer and the consequent perovskite film were studied by X-Ray Diffractometry (XRD), Atomic Force Microscopy (AFM) and Scanning Electron Microscopy (SEM). As shown in Figure S1a, the vacuum deposited PbI_2 film (thickness = 250 nm) demonstrates 3 diffraction peaks at $2\theta = 12.7°$, 25.5° and 38.6° belonging to the (100), (011), and (110) PbI_2 crystal planes, respectively. The PbI_2 layers deposited at different rates share similar XRD patterns. The dominant (100) planar orientation is indicative of the preferential growth of PbI_2 grains perpendicular to the c-axis[47] . This is further shown by SEM images in Figure S1b-d, where the PbI_2 layer is in the form of smooth platelets packed along the horizontal plane irrespective of the deposition rate. However, according to AFM measurements in Figure S2a-d, the surface roughness of PbI_2 film increases slightly from Root Mean Square (RMS) values of 2.7 to 4.0 nm as the deposition rate is changed from 2.0 to 3.5 Å/s, respectively.

The perovskite layer was subsequently formed by spin-casting MA-halide solution containing MAI, MABr, and MACl to form MAPI-BrCl. According to Figure 3a, when PbI_2 is deposited at 2.0 Å/s, there exists a PbI_2 diffraction peak at $2\theta = 12.7^\circ$ in the diffractogram of the perovskite implying that the final perovskite layer is PbI_2 rich. However, the same peak is suppressed when the initial PbI_2 is sublimed at 2.5 Å/s, and it is completely eliminated when the deposition rate of PbI_2 is further increased to 3.5 Å/s, as shown in Figure 3a. This is attributed to the increased roughness of PbI_2 deposited at high rates (Figure S2d) and hence there are more defects at which the reaction between MA-halide and PbI_2 platelets can be initiated. In addition, as the deposition rate increases, the resultant film is likely to be more porous allowing for better impregnation of the MA-halides into the PbI_2 film. The surface and cross-sectional view of the perovskite layers depending on the initial deposition rate of Pbl_2 are shown in SEM images in Figure 3b-g. The thickness of the final perovskite layer is 350 nm in all the samples. They present directional grains or boundaries which can hinder the charge carrier collection in the vertical orientation, a benchmark of MACl incorporation during perovskite fabrication[48] . However, the surface morphology changes depending on the deposition rate of the initial PbI_2 layer. When the PbI_2 rate is 2.0 Å/s, bright platelets remain at the surface of the final perovskite (Figure 3b and 3c) which we speculate to be due to residual unreacted PbI_2, since heavy-atom regions appear with brighter contrast in the SEM images[49] . This is in line with the XRD analysis in Figure 3a, which shows a more intense PbI_2 peak when the deposition rate is 2.0 Å/s. The white flakes are in the form of scattered platelets throughout the surface. The perovskite layers formed out of PbI_2 deposited at higher rates of 2.5 and 3.5 Å/s are compact with micro-scale grains as demonstrated in Figures 3d-g. Bright regions are also detectable with higher rates of 2.5 and 3.5 Å/s shown with circles on the SEM images. Nevertheless, the number of PbI_2 platelets reduces with the

deposition rate. Collectively, these results indicate more intercalation of PbI_2 with organic components as the deposition rate of PbI_2 increases.

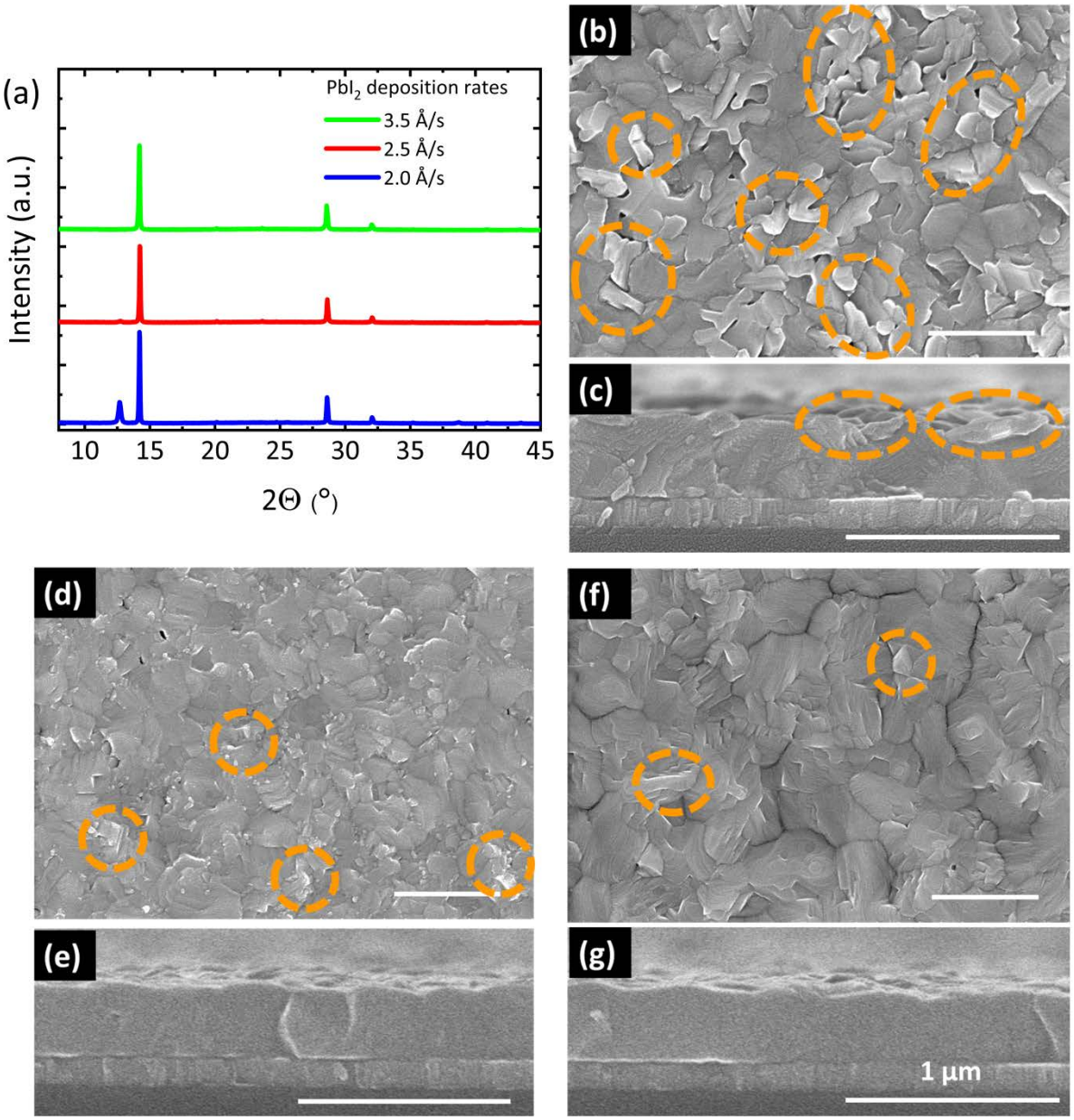

Figure 3. a) XRD pattern of MAPI-BrCl layers obtained from PbI_2 layers that were deposited at different rates. SEM surface and cross-sectional images of perovskites after conversion of PbI_2 layers at rates of (b, c) 2.0 Å/s, (d, e) 2.5 Å/s, (f, g) 3.5 Å/s.

The current density–voltage (J–V) curves and the statistics of the extracted key performance indicators are summarized in Figure 4, Figure S3, and Table 2. The highest average and record open-circuit voltages are 1102.7 mV and 1117.0 mV, respectively and were achieved for the lowest PbI_2 deposition rate of 2.0 Å/s. This is correlated with the excess unreacted PbI_2 at the interfaces of perovskite, which has been shown to passivate nonradiative recombination centers[46,50,51] . On one hand, as the deposition rate of PbI_2 increased from 2.0 to 3.5 Å/s, the average V_{OC} dropped monotonically from 1102.7 to 1020.8 mV as shown in Figure S3a. On the other hand, the average short circuit current (J_{SC}) increased from 20.3 to 21.7 mA/cm^2 as the deposition rate of PbI_2 increased from 2.0 to 2.5 Å/s and dropped slightly (0.2 mA/cm^2) when the deposition rate was 3.5 Å/s as shown in Figure S3b. The increase in J_{SC} is likely because of a more complete conversion of the PbI_2 into perovskite as evidenced by the XRD analysis in Figure 3a. Above all, the highest average fill factor (FF = 77.4%) was measured when the deposition rate was 2.5 Å/s for PbI_2. As a result, the highest average efficiency of 18.1% and lowest parameter scattering were achieved when the sublimation rate of PbI_2 was 2.5 Å/s. At this rate, a high reproducibility was obtained as indicated in by the data depicted in Figure S3. When the deposition rate was 3.5 Å/s, there seemed to be a higher leakage current according to the dark J–V curves presented in Figure 4b. This is rationalized by the formation of PbI_2 deficient perovskite as seen in Figure 3f-g. Excess PbI_2 as in the case of lower PbI_2 rates, can passivate the perovskite film and facilitate charge transportation[46,49,50] . Also, excess PbI_2 has been demonstrated to block the shunt paths. Thus, due to complete consumption of PbI_2 deposited at 3.5 Å/s, there are more shunt paths in the subsequent solar cell causing poor FF in the J–V curve[52]. As a result, considering the highest efficiencies and reproducibility, the deposition rate of PbI_2 was kept constant at 2.5 Å/s in the following sections.

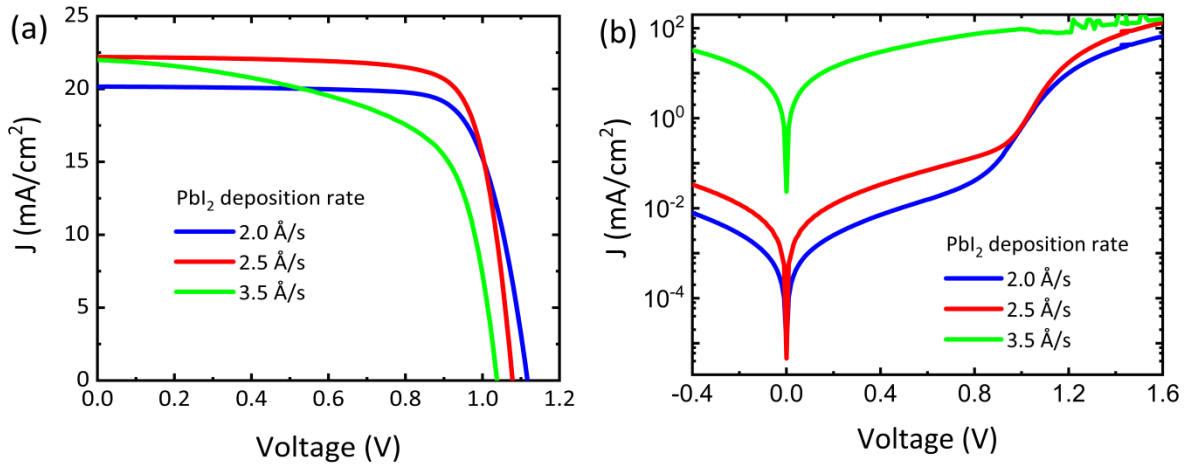

Figure 4. a) J–V curves for the best devices of MAPI-BrCl made from PbI_2 deposited at different evaporation rates. b) Dark J–V parameters for the best devices shown in a).

Table 2. Key performance parameters extracted from the J–V curves for the devices made using PbI_2 layers deposited at different evaporation rates.

PbI_2 deposition rate (Å/s)	V_{OC} (mV)	J_{SC} (mA/cm^2)	FF (%)	PCE (%)
2.0	1117.0	20.2	76.7	17.3
2.5	1078.0	22.2	78.0	18.7
3.5	1042.3	22.0	73.2	16.8

In addition to the PbI_2 evaporation rate, the MA-halide solution was further optimized addressing the minimum fluctuation in the performance parameters of the solar cells. When a higher concentration of MABr (20 mg/ml instead of 10 mg/ml) was used in the MA-halide solution, the resultant perovskite layer became a poor absorber as can be seen in Figure S4a, b. The spectral photo-response of the device diminished drastically followed by a serious drop in the power conversion efficiency from 19.3% to 4.5% as shown in Figure S4b, c and Table S2. A

similar effect was observed when the concentration of MACl was increased from 5 mg/ml to 10 mg/ml in combination with MABr (10 mg/ml). The solar cells, incorporating the perovskite film prepared with the increased MACl concentration had a lower external quantum efficiency which translated into a lowering of the J_{SC} (by 2.5 mA/cm^2) and also a 3.1% lower power conversion efficiency as compared to the reference cell. The results have been summarized in Figure S4 and Table S2. This is also in line with a previous study related to the MACl concentration[47]. These results demonstrate that the improvements in the conversion of perovskite layer and subsequent device performance are not the result of a higher MA+ concentration, but rather a result of the mixed halides used. To verify if further improvements in device performance are feasible, we investigated the MABr/MAI molar ratio with small step sizes. The MABr/MAI molar ratio was varied from 0.36 to 0.41, 0.46, 0.51, 0.56, 0.61 and 0.71. Increasing the ratio from 0.36 to 0.71 shifted the absorbance edge from 755 (1.64 eV) to 730 nm (1.7 eV) as shown in Figure 5a. According to Figure S5, the amplitude of the blue shift in the bandgap was not linear and varied with the molar ratio of MABr/MAI. The average associated V_{OC} increased from 1083.9 mV to a maximum value of 1136.7 mV as the MABr/MAI molar ratio increased from 0.36 to 0.56 (Figure 6), in agreement with the trend for the expected values based on Shockley-Queisser (SQ) limit at the associated bandgap of every MABr/MAI ratio (Figure S6). However, the magnitude of the difference between the SQ and average values (V_{OC}^{SQ} - V_{OC}^{AVE}) shown in Figure S7, increased more as the MABr/MAI ratio increased from 0.41 to 0.51. When the ratio was further increased to 0.71, not only the average V_{OC} dropped from 1136.7 to 1114.9 mV but also, V_{OC}^{SQ} - V_{OC}^{AVE} increased. Since the minimum value of V_{OC}^{SQ} - V_{OC}^{AVE} obtained corresponds to devices employing perovskites prepared from a conversion solution with a MABr/MAI ratio of 0.41, the non-radiative recombinations are most reduced at this ratio. On the other hand, the trends in the

average J_{SC}, FF, and PCE also follow the predicted SQ trends based on the bandgap for the perovskites prepared with the different MABr/MAI ratio in the conversion solution (Figure S6). The highest average J_{SC} (20.8 mA/cm^2) and FF (80.7%) were measured when the ratio was 0.41 and 0.61, respectively. The best performing solar cells are obtained with conversion solutions with the MABr/MAI ratio of 0.41. At these same preparation conditions also, the solar cells showed the least spreading in performance data (Figures 6 and S7). The best average efficiency (18.7%) and record efficiency (19.8%) were achieved when the ratio was equal to 0.41, as depicted in Figure 5b.

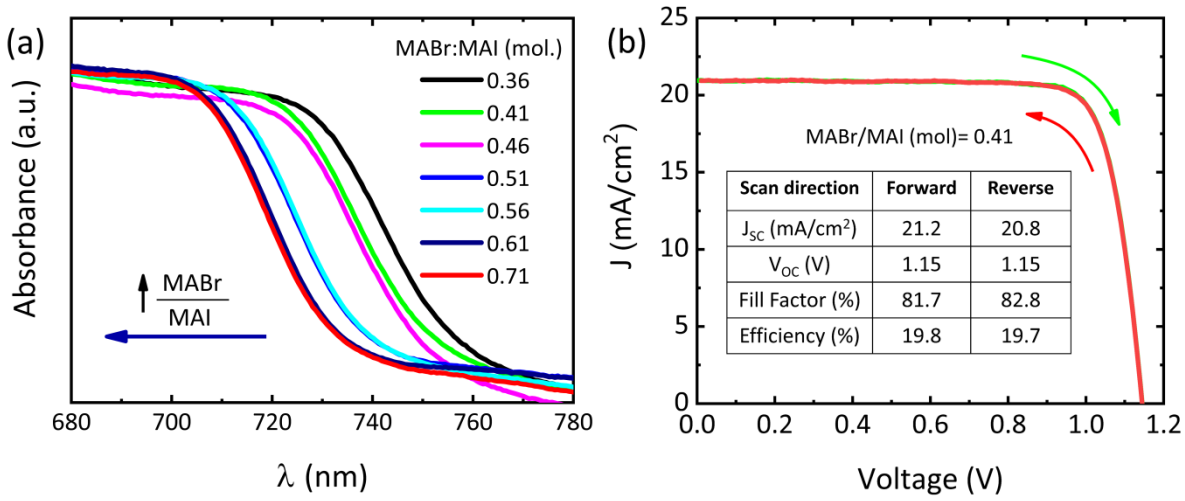

Figure 5. a) Absorbance spectra of MAPI-BrCl for different MABr:MAI molar ratio in the MA-halide solution. b) The J–V characteristic curve for the champion cell with an MABr/MAI molar ratio of 0.41.

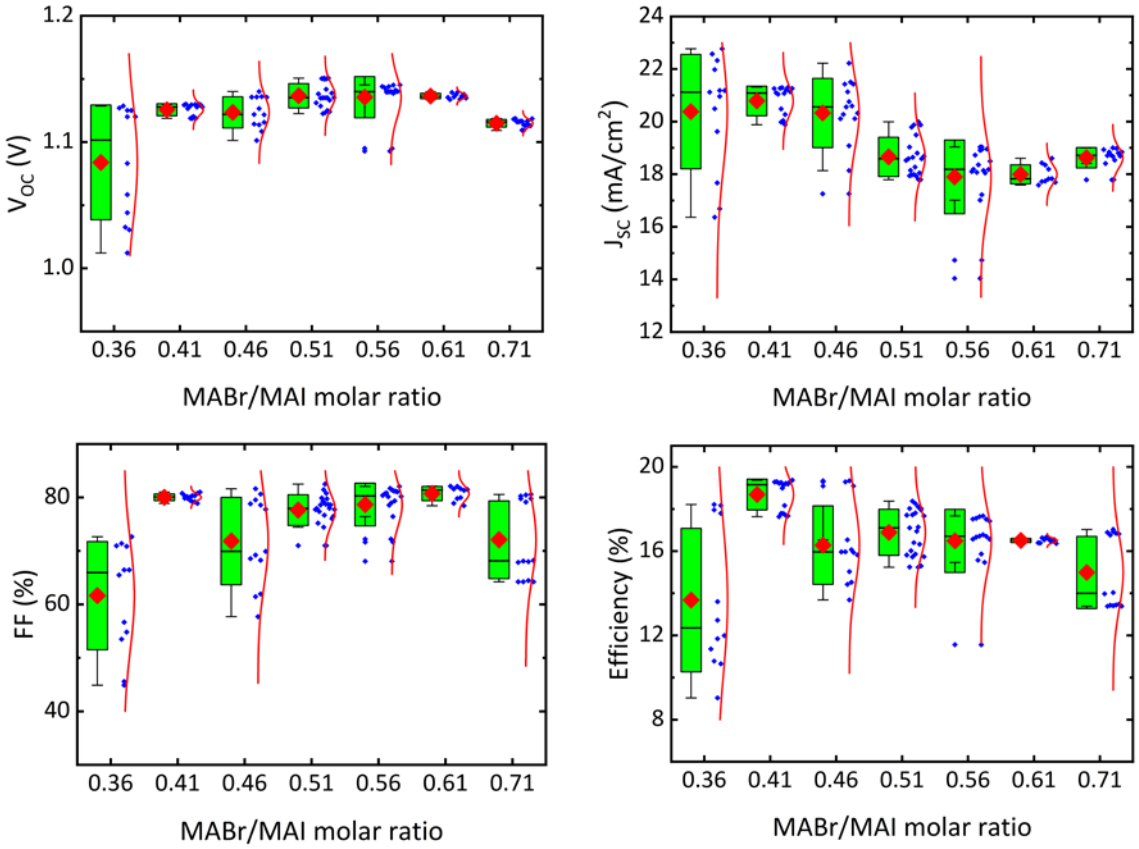

Figure 6. Photovoltaic parameters of the MAPI-BrCl solar cells made with different MABr:MAI molar ratios between 0.36 to 0.71 in the MA solution. The amount of MACl was kept constant in all solutions. At least 6 solar cells were measured in each category.

3.3 Stability Analysis

To evaluate the stability of the MAPI-Br, MAPI-Cl, and MAPI-BrCl solar cells, they were encapsulated following a method described in the experimental section. The performance versus time of the encapsulated devices was measured tracking J–V characteristics of the devices every 15 minutes under constant 1 Sun illumination while held at room temperature in the air. The results are shown in Figure S8. MAPI-Br and MAPI-BrCl respectively demonstrated maximum stability in all the J–V characteristic data with a 6% and 10% increase of their starting efficiency

over 90 hours of constant operation. Conversely, MAPI-Cl turned out to be unstable due to J_{SC} and FF loss over time. So, despite the enhanced crystallization of perovskite and improved efficiencies of MAPI-Cl, the exclusion of Br^- was at the expense of stability especially in the FF of the devices. In short, in view of the J–V data and stability analyses, the incorporation of both Br^- and Cl^- in the MA-halide solution was found to be optimal in achieving the best device performance as well as sustaining the device stability under working conditions which is in agreement with the previous studies[33] .

4. Conclusion

Using a combination of vacuum and solution processing to prepare lead iodide based perovskites efficient and stable p-i-n type solar cells were obtained that did not show hysteresis. Uniform perovskite layers were obtained due to the use of vapor deposition for the inorganic PbI_2 layer which determines the position and uniformity of the final perovskite. To prevent hysteresis as much as possible the PbI_2 layer was grown on a thin amorphous organic hole transport layer. This leads to dense PbI_2 layers that are not easily converted to perovskite. The addition of Br^- and Cl^- into the MA-halide conversion solution during the second step ensured an efficient permeation of MA-halide compounds into the dense PbI_2 film. It also provided an effective control over the crystallization of the perovskite resulting in perpendicular grains spanning the complete distance from hole to electron extraction layers. Using this protocol p-i-n type solar cells were obtained with a high reproducibility reaching power conversion efficiencies as high as 19.8% and a stability in excess of 90 hours.

ASSOCIATED CONTENT

Supporting Information.

XRD, AFM, and, SEM of the PbI_2 layer deposited at different rates, device statistical data depending on PbI_2 deposition rate, XRD of MAPI-BrCl depending on MACl concentration, the effect of MABr/MAI ratio on the absorbance edge and on the Shockley-Queisser limit and average values of J–V parameters, stability analysis of the devices.

AUTHOR INFORMATION

Corresponding Author

* E-mail: henk.bolink@uv.es

* E-mail: syerci@metu.edu.tr

* E-mail: Pablo.P.Boix@uv.es

* E-mail: ggunbas@metu.edu.tr

Acknowledgements

We are grateful to Prof. Juan Martínez-Pastor for providing the opportunity to measure the photoluminescence spectra of our samples on a femtosecond laser setup.

Funding Sources

The research leading to these results has received funding from the Spanish Ministry of Science, Innovation and Universities MAT2017-88821-R, EQC2018-004888-P Comunitat Valenciana IDIFEDER/2018/061). The project was also funded by the Scientific and Technological Research Council of Turkey (TÜBITAK) under contract number of 315M360.

5. REFERENCES

(1) Green, M. A.; Dunlop, E. D.; Levi, D. H.; Hohl-Ebinger, J.; Yoshita, M.; Ho-Baillie, A. W. Y. Solar Cell Efficiency Tables (Version 54). Prog. Photovoltaics Res. Appl. 2019, 27 (7), 565–575. https://doi.org/10.1002/pip.3171.

(2) Noh, J. H.; Im, S. H.; Heo, J. H.; Mandal, T. N.; Seok, S. Il. Chemical Management for Colorful, Efficient, and Stable Inorganic-Organic Hybrid Nanostructured Solar Cells. Nano Lett. 2013, 13 (4), 1764–1769. https://doi.org/10.1021/nl400349b.

(3) Smith, M. D.; Connor, B. A.; Karunadasa, H. I. Tuning the Luminescence of Layered Halide Perovskites. Chemical Reviews. American Chemical Society March 13, 2019, pp 3104–3139. https://doi.org/10.1021/acs.chemrev.8b00477.

(4) Lin, Q.; Armin, A.; Nagiri, R. C. R.; Burn, P. L.; Meredith, P. Electro-Optics of Perovskite Solar Cells. Nat. Photonics 2015, 9 (2), 106–112. https://doi.org/10.1038/nphoton.2014.284.

(5) Miyata, A.; Mitioglu, A.; Plochocka, P.; Portugall, O.; Wang, J. T. W.; Stranks, S. D.; Snaith, H. J.; Nicholas, R. J. Direct Measurement of the Exciton Binding Energy and Effective Masses for Charge Carriers in Organic-Inorganic Tri-Halide Perovskites. Nat. Phys. 2015, 11 (7), 582–587. https://doi.org/10.1038/nphys3357.

(6) Stranks, S. D.; Eperon, G. E.; Grancini, G.; Menelaou, C.; Alcocer, M. J. P.; Leijtens, T.; Herz, L. M.; Petrozza, A.; Snaith, H. J. Electron-Hole Diffusion Lengths Exceeding 1 Micrometer in an Organometal Trihalide Perovskite Absorber. Science (80-.). 2013, 342 (6156), 341–344. https://doi.org/10.1126/science.1243982.

(7) Lee, J.-W.; Kim, D.-H.; Kim, H.-S.; Seo, S.-W.; Cho, S. M.; Park, N.-G. Formamidinium and Cesium Hybridization for Photo- and Moisture-Stable Perovskite Solar Cell. Adv. Energy Mater. 2015, 5 (20), 1501310. https://doi.org/10.1002/aenm.201501310.

(8) Saliba, M.; Matsui, T.; Seo, J. Y.; Domanski, K.; Correa-Baena, J. P.; Nazeeruddin, M. K.; Zakeeruddin, S. M.; Tress, W.; Abate, A.; Hagfeldt, A.; Grätzel, M. Cesium-Containing Triple Cation Perovskite Solar Cells: Improved Stability, Reproducibility and High Efficiency. Energy Environ. Sci. 2016, 9 (6), 1989–1997. https://doi.org/10.1039/c5ee03874j.

(9) Yi, C.; Luo, J.; Meloni, S.; Boziki, A.; Ashari-Astani, N.; Grätzel, C.; Zakeeruddin, S. M.; Röthlisberger, U.; Grätzel, M. Entropic Stabilization of Mixed A-Cation ABX3 Metal Halide Perovskites for High Performance Perovskite Solar Cells. Energy Environ. Sci. 2016, 9 (2), 656–662. https://doi.org/10.1039/c5ee03255e.

(10) Rehman, W.; McMeekin, D. P.; Patel, J. B.; Milot, R. L.; Johnston, M. B.; Snaith, H. J.; Herz, L. M. Photovoltaic Mixed-Cation Lead Mixed-Halide Perovskites: Links between Crystallinity, Photo-Stability and Electronic Properties. Energy Environ. Sci. 2017, 10 (1), 361–369. https://doi.org/10.1039/c6ee03014a.

(11) Swarnkar, A.; Mir, W. J.; Nag, A. Can B-Site Doping or Alloying Improve Thermal- and Phase-Stability of All-Inorganic CsPbX 3 (X = Cl, Br, I) Perovskites? ACS Energy Lett. 2018, 3 (2), 286–289. https://doi.org/10.1021/acsenergylett.7b01197.

(12) Xiao, M.; Huang, F.; Huang, W.; Dkhissi, Y.; Zhu, Y.; Etheridge, J.; Gray-Weale, A.; Bach, U.; Cheng, Y.-B.; Spiccia, L. A Fast Deposition-Crystallization Procedure for Highly

Efficient Lead Iodide Perovskite Thin-Film Solar Cells. Angew. Chemie Int. Ed. 2014, 53 (37), 9898–9903. https://doi.org/10.1002/anie.201405334.

(13) Li, Z.; Klein, T. R.; Kim, D. H.; Yang, M.; Berry, J. J.; Van Hest, M. F. A. M.; Zhu, K. Scalable Fabrication of Perovskite Solar Cells. Nature Reviews Materials. Nature Publishing Group March 27, 2018. https://doi.org/10.1038/natrevmats.2018.17.

(14) Im, J. H.; Jang, I. H.; Pellet, N.; Grätzel, M.; Park, N. G. Growth of CH3 NH3 PbI3 Cuboids with Controlled Size for High-Efficiency Perovskite Solar Cells. Nat. Nanotechnol. 2014, 9 (11), 927–932. https://doi.org/10.1038/nnano.2014.181.

(15) Burschka, J.; Pellet, N.; Moon, S. J.; Humphry-Baker, R.; Gao, P.; Nazeeruddin, M. K.; Grätzel, M. Sequential Deposition as a Route to High-Performance Perovskite-Sensitized Solar Cells. Nature 2013, 499 (7458), 316–319. https://doi.org/10.1038/nature12340.

(16) Yantara, N.; Sabba, D.; Yanan, F.; Kadro, J. M.; Moehl, T.; Boix, P. P.; Mhaisalkar, S.; Grätzel, M.; Grätzel, C. Loading of Mesoporous Titania Films by CH 3 NH 3 PbI 3 Perovskite, Single Step vs. Sequential Deposition. Chem. Commun. 2015, 51 (22), 4603–4606. https://doi.org/10.1039/C4CC09556A.

(17) Pérez-del-Rey, D.; Boix, P. P.; Sessolo, M.; Hadipour, A.; Bolink, H. J. Interfacial Modification for High-Efficiency Vapor-Phase-Deposited Perovskite Solar Cells Based on a Metal Oxide Buffer Layer. J. Phys. Chem. Lett. 2018, 9 (5), 1041–1046. https://doi.org/10.1021/acs.jpclett.7b03361.

(18) Momblona, C.; Gil-Escrig, L.; Bandiello, E.; Hutter, E. M.; Sessolo, M.; Lederer, K.; Blochwitz-Nimoth, J.; Bolink, H. J. Efficient Vacuum Deposited P-i-n and n-i-p Perovskite Solar

Cells Employing Doped Charge Transport Layers. Energy Environ. Sci. 2016, 9 (11), 3456–3463. https://doi.org/10.1039/c6ee02100j.

(19) Hsiao, S.-Y.; Lin, H.-L.; Lee, W.-H.; Tsai, W.-L.; Chiang, K.-M.; Liao, W.-Y.; Ren-Wu, C.-Z.; Chen, C.-Y.; Lin, H.-W. Efficient All-Vacuum Deposited Perovskite Solar Cells by Controlling Reagent Partial Pressure in High Vacuum. Adv. Mater. 2016, 28 (32), 7013–7019. https://doi.org/10.1002/adma.201601505.

(20) Chen, C.-W.; Kang, H.-W.; Hsiao, S.-Y.; Yang, P.-F.; Chiang, K.-M.; Lin, H.-W. Efficient and Uniform Planar-Type Perovskite Solar Cells by Simple Sequential Vacuum Deposition. Adv. Mater. 2014, 26 (38), 6647–6652. https://doi.org/10.1002/adma.201402461.

(21) Fu, F.; Kranz, L.; Yoon, S.; Löckinger, J.; Jäger, T.; Perrenoud, J.; Feurer, T.; Gretener, C.; Buecheler, S.; Tiwari, A. N. Controlled Growth of PbI 2 Nanoplates for Rapid Preparation of CH 3 NH 3 PbI 3 in Planar Perovskite Solar Cells. Phys. Status Solidi Appl. Mater. Sci. 2015, 212 (12), 2708–2717. https://doi.org/10.1002/pssa.201532442.

(22) Duan, J.; Liu, Z.; Zhang, Y.; Liu, K.; He, T.; Wang, F.; Dai, J.; Zhou, P. Planar Perovskite FAxMA1-XPbI3 Solar Cell by Two-Step Deposition Method in Air Ambient. Opt. Mater. (Amst). 2018, 85, 55–60. https://doi.org/10.1016/j.optmat.2018.07.072.

(23) Bing, J.; Kim, J.; Zhang, M.; Zheng, J.; Lee, D. S.; Cho, Y.; Deng, X.; Lau, C. F. J.; Li, Y.; Green, M. A.; Huang, S.; Ho-Baillie, A. W. Y. The Impact of a Dynamic Two-Step Solution Process on Film Formation of Cs 0.15 (MA 0.7 FA 0.3) 0.85 PbI 3 Perovskite and Solar Cell Performance. Small 2019, 15 (9), 1804858. https://doi.org/10.1002/smll.201804858.

(24) Hwang, K.; Jung, Y.-S.; Heo, Y.-J.; Scholes, F. H.; Watkins, S. E.; Subbiah, J.; Jones, D. J.; Kim, D.-Y.; Vak, D. Toward Large Scale Roll-to-Roll Production of Fully Printed Perovskite Solar Cells. Adv. Mater. 2015, 27 (7), 1241–1247. https://doi.org/10.1002/adma.201404598.

(25) Huang, H.; Shi, J.; Zhu, L.; Li, D.; Luo, Y.; Meng, Q. Two-Step Ultrasonic Spray Deposition of CH3NH3PbI3 for Efficient and Large-Area Perovskite Solar Cell. Nano Energy 2016, 27, 352–358. https://doi.org/10.1016/j.nanoen.2016.07.026.

(26) Rafizadeh, S.; Wienands, K.; Schulze, P. S. C.; Bett, A. J.; Andreani, L. C.; Hermle, M.; Glunz, S.; Goldschmidt, J. C. Efficiency Enhancement and Hysteresis Mitigation by Manipulation of Grain Growth Conditions in Hybrid Evaporated−Spin-Coated Perovskite Solar Cells. 2018. https://doi.org/10.1021/acsami.8b16963.

(27) Unger, E. L.; Hoke, E. T.; Bailie, C. D.; Nguyen, W. H.; Bowring, A. R.; Heumüller, T.; Christoforo, M. G.; McGehee, M. D. Hysteresis and Transient Behavior in Current-Voltage Measurements of Hybrid-Perovskite Absorber Solar Cells. Energy Environ. Sci. 2014, 7 (11), 3690–3698. https://doi.org/10.1039/c4ee02465f.

(28) Yang, D.; Zhou, X.; Yang, R.; Yang, Z.; Yu, W.; Wang, X.; Li, C.; Liu, S.; Chang, R. P. H. Surface Optimization to Eliminate Hysteresis for Record Efficiency Planar Perovskite Solar Cells. Energy Environ. Sci. 2016, 9 (10), 3071–3078. https://doi.org/10.1039/c6ee02139e.

(29) Byranvand, M. M.; Kim, T.; Song, S.; Kang, G.; Ryu, S. U.; Park, T. P-Type CuI Islands on TiO 2 Electron Transport Layer for a Highly Efficient Planar-Perovskite Solar Cell with Negligible Hysteresis. Adv. Energy Mater. 2018, 8 (5), 1702235. https://doi.org/10.1002/aenm.201702235.

(30) Li, Y.; Zhao, Y.; Chen, Q.; Yang, Y.; Liu, Y.; Hong, Z.; Liu, Z.; Hsieh, Y. T.; Meng, L.; Li, Y.; Yang, Y. Multifunctional Fullerene Derivative for Interface Engineering in Perovskite Solar Cells. J. Am. Chem. Soc. 2015, 137 (49), 15540–15547. https://doi.org/10.1021/jacs.5b10614.

(31) Sidhik, S.; Panikar, S. S.; Pérez, C. R.; Luke, T. L.; Carriles, R.; Carrera, S. C.; De la Rosa, E. Interfacial Engineering of TiO 2 by Graphene Nanoplatelets for High-Efficiency Hysteresis-Free Perovskite Solar Cells. ACS Sustain. Chem. Eng. 2018, 6 (11), 15391–15401. https://doi.org/10.1021/acssuschemeng.8b03826.

(32) Luo, J.; Wan, Z.; Han, F.; Malik, H. A.; Zhao, B.; Xia, J.; Jia, C.; Wang, R. Origin of Increased Efficiency and Decreased Hysteresis of Perovskite Solar Cells by Using 4-Tert-Butyl Pyridine as Interfacial Modifier for TiO2. J. Power Sources 2019, 415, 197–206. https://doi.org/10.1016/j.jpowsour.2019.01.064.

(33) Sun, Z.; Huang, W.; Ma, H.; Lv, Y.; Wang, J.; Zhang, H. Influence of Cl Incorporation in Perovskite Precursor on the Crystal Growth and Storage Stability of Perovskite Solar Cells. ACS Appl. Mater. Interfaces 2019, 11, 6, 6022. https://doi.org/10.1021/acsami.8b19390.

(34) Song, L.; Wang, W.; Körstgens, V.; Moseguí González, D.; Löhrer, F. C.; Schaffer, C. J.; Schlipf, J.; Peters, K.; Bein, T.; Fattakhova-Rohlfing, D.; Roth, S. V.; Müller-Buschbaum, P. In Situ Study of Spray Deposited Titania Photoanodes for Scalable Fabrication of Solid-State Dye-Sensitized Solar Cells. Nano Energy 2017, 40, 317–326. https://doi.org/10.1016/J.NANOEN.2017.08.023.

(35) Ummadisingu, A.; Grätzel, M. Revealing the Detailed Path of Sequential Deposition for Metal Halide Perovskite Formation. Sci. Adv. 2018, 4 (2), e1701402. https://doi.org/10.1126/sciadv.1701402.

(36) Liu, D.; Gangishetty, M. K.; Kelly, T. L. Effect of CH 3 NH 3 PbI 3 Thickness on Device Efficiency in Planar Heterojunction Perovskite Solar Cells. J. Mater. Chem. A 2014, 2 (46), 19873–19881. https://doi.org/10.1039/C4TA02637C.

(37) Tripathi, N.; Yanagida, M.; Shirai, Y.; Miyano, K. Improved Performance of Planar Perovskite Devices via Inclusion of Ammonium Acid Iodide (AAI) Derivatives Using a Two Step Inter-Diffusion Process. J. Mater. Chem. C 2019, 7 (12), 3447–3451. https://doi.org/10.1039/c8tc05328f.

(38) Li, M.; Yan, X.; Kang, Z.; Liao, X.; Li, Y.; Zheng, X.; Lin, P.; Meng, J.; Zhang, Y. Enhanced Efficiency and Stability of Perovskite Solar Cells via Anti-Solvent Treatment in Two-Step Deposition Method. 2017. https://doi.org/10.1021/acsami.7b01136.

(39) Chen, H.; Wei, Z.; He, H.; Zheng, X.; Wong, K. S.; Yang, S. Solvent Engineering Boosts the Efficiency of Paintable Carbon-Based Perovskite Solar Cells to Beyond 14%. Adv. Energy Mater. 2016, 6 (8), 1502087. https://doi.org/10.1002/aenm.201502087.

(40) Dong, Q.; Yuan, Y.; Shao, Y.; Fang, Y.; Wang, Q.; Huang, J. Abnormal Crystal Growth in CH 3 NH 3 PbI 3−x Cl x Using a Multi-Cycle Solution Coating Process. Energy Environ. Sci. 2015, 8 (8), 2464–2470. https://doi.org/10.1039/C5EE01179E.

(41) Chen, Q.; Zhou, H.; Fang, Y.; Stieg, A. Z.; Song, T. Bin; Wang, H. H.; Xu, X.; Liu, Y.; Lu, S.; You, J.; Sun, P.; McKay, J.; Goorsky, M. S.; Yang, Y. The Optoelectronic Role of

Chlorine in CH3NH3PbI3 (Cl)-Based Perovskite Solar Cells. Nat. Commun. 2015, 6, 7269. https://doi.org/10.1038/ncomms8269.

(42) Ono, L. K.; Juarez-Perez, E. J.; Qi, Y. Progress on Perovskite Materials and Solar Cells with Mixed Cations and Halide Anions. ACS Appl. Mater. Interfaces 2017, 9 (36), 30197–30246. https://doi.org/10.1021/acsami.7b06001.

(43) Yoon, S. J.; Stamplecoskie, K. G.; Kamat, P. V. How Lead Halide Complex Chemistry Dictates the Composition of Mixed Halide Perovskites. J. Phys. Chem. Lett. 2016, 7 (7), 1368–1373. https://doi.org/10.1021/acs.jpclett.6b00433.

(44) Song, T. Bin; Chen, Q.; Zhou, H.; Jiang, C.; Wang, H. H.; Yang, Y. M.; Liu, Y.; You, J.; Yang, Y. Perovskite Solar Cells: Film Formation and Properties. J. Mater. Chem. A 2015, 3 (17), 9032–9050. https://doi.org/10.1039/c4ta05246c.

(45) Xu, J.; Boyd, C. C.; Yu, Z. J.; Palmstrom, A. F.; Witter, D. J.; Larson, B. W.; France, R. M.; Werner, J.; Harvey, S. P.; Wolf, E. J.; Weigand, W.; Manzoor, S.; A M van Hest, M. F.; Berry, J. J.; Luther, J. M.; Holman, Z. C.; McGehee, M. D. Triple-Halide Wide-Band Gap Perovskites with Suppressed Phase Segregation for Efficient Tandems Downloaded From; 2020; Vol. 367.

(46) Bae, D.; Palmstrom, A.; Roelofs, K.; Mei, B.; Chorkendorff, I.; Bent, S. F.; Vesborg, P. C. K. Tailoring Mixed-Halide, Wide-Gap Perovskites via Multistep Conversion Process. ACS Appl. Mater. Interfaces 2016, 8 (23), 14301–14306. https://doi.org/10.1021/acsami.6b01246.

(47) Yang, L.; Barrows, A. T.; Lidzey, D. G. PbI 2 Platelets for Inverted Planar Organolead Halide Perovskite Solar Cells via Ultrasonic Spray Deposition Related Content Recent Progress

and Challenges of Organometal Halide Perovskite Solar Cells. 2017. https://doi.org/10.1088/1361-6641/aa6e47.

(48) Xie, F.; Chen, C. C.; Wu, Y.; Li, X.; Cai, M.; Liu, X.; Yang, X.; Han, L. Vertical Recrystallization for Highly Efficient and Stable Formamidinium-Based Inverted-Structure Perovskite Solar Cells. Energy Environ. Sci. 2017, 10 (9), 1942–1949. https://doi.org/10.1039/c7ee01675a.

(49) Jiang, Q.; Chu, Z.; Wang, P.; Yang, X.; Liu, H.; Wang, Y.; Yin, Z.; Wu, J.; Zhang, X.; You, J. Planar-Structure Perovskite Solar Cells with Efficiency beyond 21%. Adv. Mater. 2017, 29 (46), 1–7. https://doi.org/10.1002/adma.201703852.

(50) Chen, Q.; Zhou, H.; Song, T.-B.; Luo, S.; Hong, Z.; Duan, H.-S.; Dou, L.; Liu, Y.; Yang, Y. Controllable Self-Induced Passivation of Hybrid Lead Iodide Perovskites toward High Performance Solar Cells. Nano Lett 2014, 14, 39. https://doi.org/10.1021/nl501838y.

(51) Zhang, T.; Guo, N.; Li, G.; Qian, X.; Zhao, Y. A Controllable Fabrication of Grain Boundary PbI2 Nanoplates Passivated Lead Halide Perovskites for High Performance Solar Cells. Nano Energy 2016, 26, 50–56. https://doi.org/10.1016/J.NANOEN.2016.05.003.

(52) Du, T.; Burgess, C. H.; Kim, J.; Zhang, J.; Durrant, J. R.; McLachlan, M. A. Formation, Location and Beneficial Role of PbI2 in Lead Halide Perovskite Solar Cells. *Sustain. Energy Fuels* **2017**, *1* (1), 119–126. https://doi.org/10.1039/c6se00029k.

Table of Contents

Supporting Information

Hybrid vapor-solution sequentially deposited mixed-halide perovskite solar cells

Wiria Soltanpoor[1,2], Chris Dreessen[3], Mehmet Cem Sahiner[1,4], Isidora Susic[3], Amir Zarean Afshord[1,2], Vladimir S. Chirvony[3,5], Pablo P. Boix[3,*], Gorkem Gunbas[1,2,6,7,*], Selcuk Yerci[1,2,4,*], Henk J. Bolink[3,*]

[1]The Center for Solar Energy Research and Applications (GUNAM), Middle East Technical University, Ankara, 06800, Turkey
[2]Department of Micro and Nanotechnology, Middle East Technical University, Ankara, 06800, Turkey
[3]Instituto de Ciencia Molecular, Universidad de Valencia, C/Catedrático J. Beltrán 2, 46980 Paterna, Spain
[4]Department of Electrical and Electronics Engineering, Middle East Technical University, Ankara, 06800, Turkey
[5] Instituto de Ciencia de Materiales, Universidad de Valencia, C/Catedrático J. Beltrán, 2, 46980 Paterna, Spain
[6]Department of Polymer Science and Technology, Middle East Technical University, Ankara, 06800, Turkey
[7]Department of Chemistry, Middle East Technical University, Ankara, 06800, Turkey

Corresponding authors:

Henk J. Bolink, * E-mail: henk.bolink@uv.es

Selcuk Yerci, * E-mail: syerci@metu.edu.tr

Pablo P. Boix, * E-mail: Pablo.P.Boix@uv.es

Gorkem Gunbas, * E-mail: ggunbas@metu.edu.tr

Table S1. The concentration of MA-halide solution in molar values. The molar ratio of MABr/MAI is 0.41 in the case of MAPI-Br and MAPI-BrCl.

	MAI (moles)	MABr(moles)	MACl(moles)
MAPI	**0.22×10^{-3}**	**0**	**0**
MAPI-Cl	**0.22×10^{-3}**	**0**	**0.09×10^{-3}**
MAPI-Br	**0.22×10^{-3}**	**0.09×10^{-3}**	**0**
MAPI-BrCl	**0.22×10^{-3}**	**0.09×10^{-3}**	**0.07×10^{-3}**

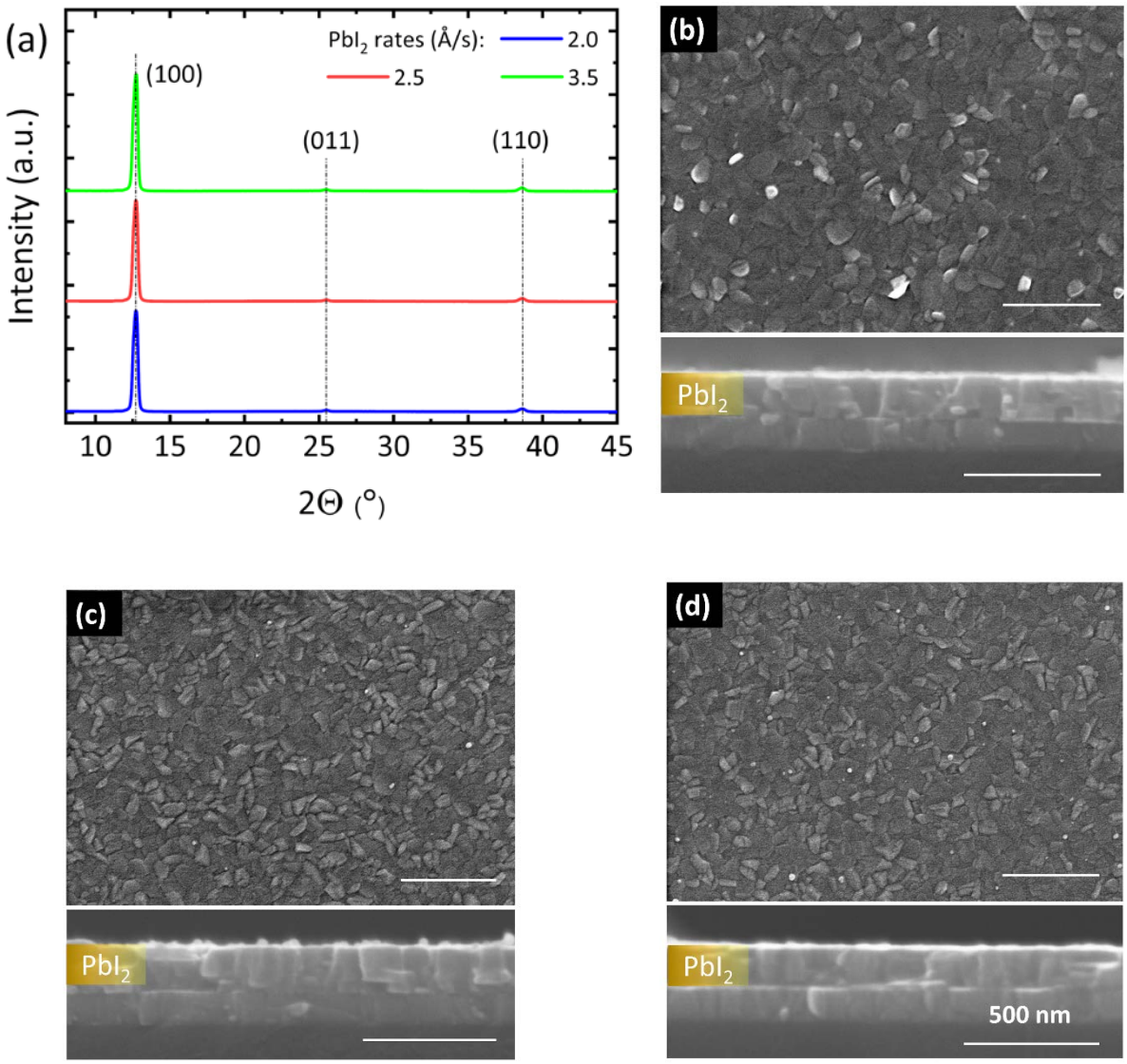

Figure S1. a) XRD patterns for the PbI_2 layer deposited at 2.0-3.5 Å/s. SEM surface images of 250 nm PbI_2 layer deposited at a) 2.0 Å/s, b) 2.5 Å/s, c) 3.5 Å/s. The insets show the cross-sectional SEM images of the related sample.

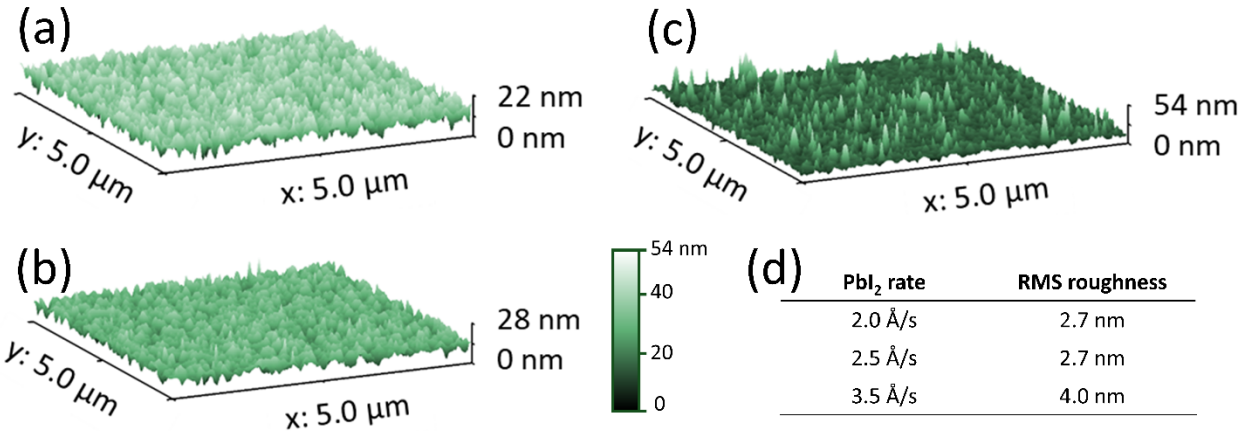

PbI_2 rate	RMS roughness
2.0 Å/s	2.7 nm
2.5 Å/s	2.7 nm
3.5 Å/s	4.0 nm

Figure S2. AFM analysis for PbI_2 layer deposited at (a) 2.0 Å/s, (b) 2.5 Å/s, (c) 3.5 Å/s. d) RMS roughness values of the PbI_2 layer shown in a-c.

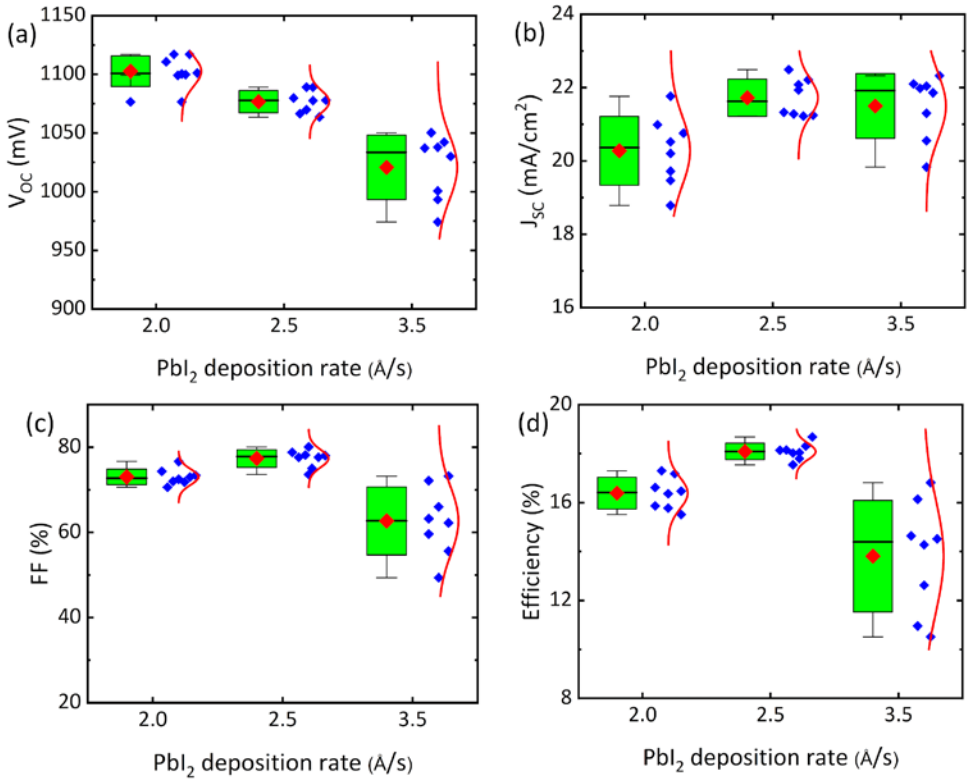

Figure S3. (a-d) The statistics of the photovoltaic parameters of the perovskite solar cells made from PbI_2 layers deposited at different evaporation rates.

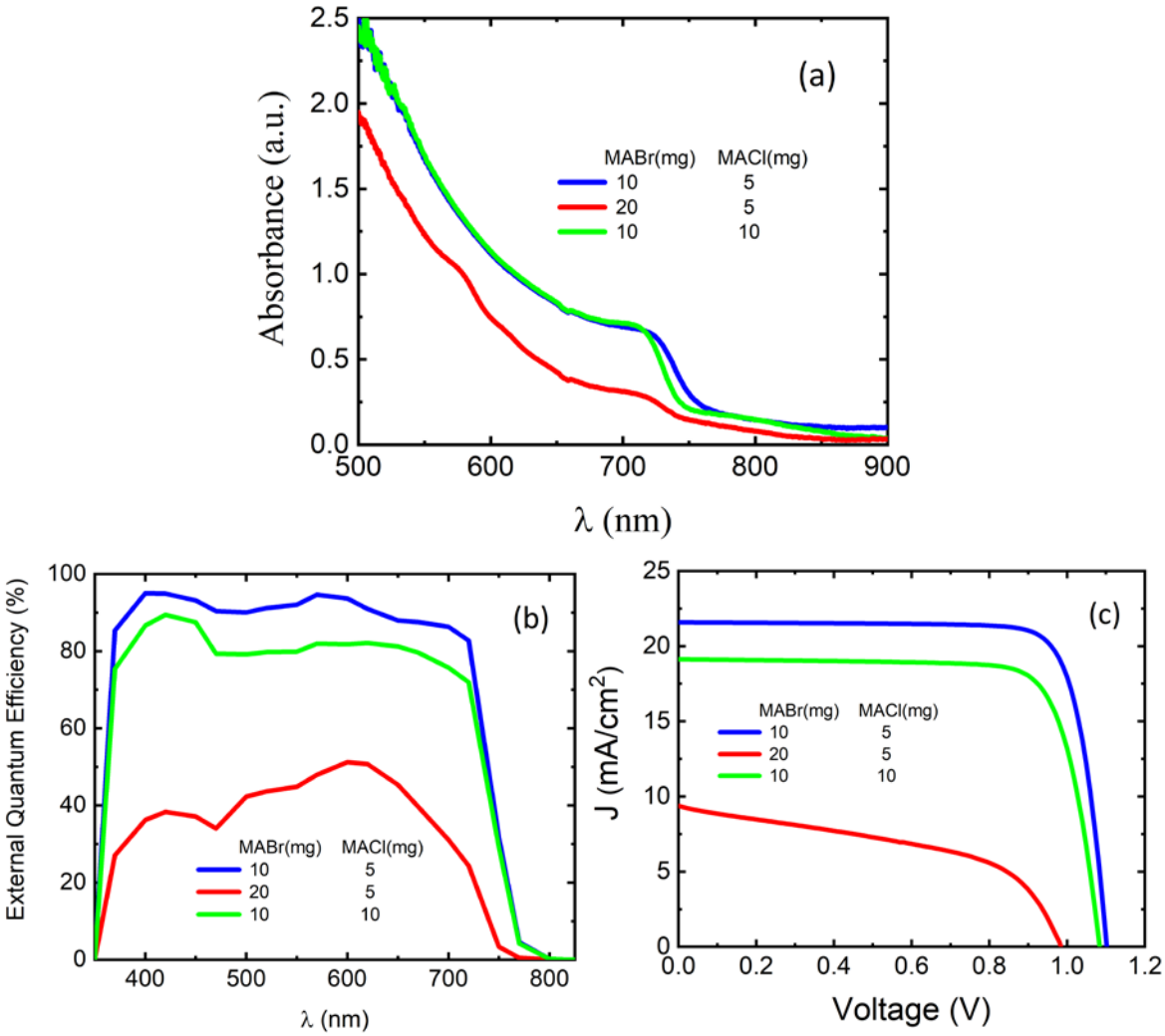

Figure S4. (a), (b), and (c) respectively show the absorbance, EQE spectra, and J-V curves of MAPI-BrCl cells when increased concentrations of MABr (20 mg/ml) and MACl (10 mg/ml) are used versus the optimized concentrations of MABr = 10 mg/ml and MACl = 5 mg/ml.

Table S2. The extracted performance parameters from J–V curves of the MAPI-BrCl solar cells when increased concentrations of MABr and MACl are used corresponding to Figure S4.

MAI(mg)	MABr(mg)	MACl(mg)	V_{OC} (mV)	J_{SC} (mA/cm^2)	FF (%)	PCE (%)
35	**10**	**5**	**1102.3**	**21.6**	**81.1**	**19.3**
35	**20**	**5**	**984.8**	**9.4**	**48.9**	**4.5**
35	**10**	**10**	**1083.7**	**19.1**	**78.4**	**16.2**

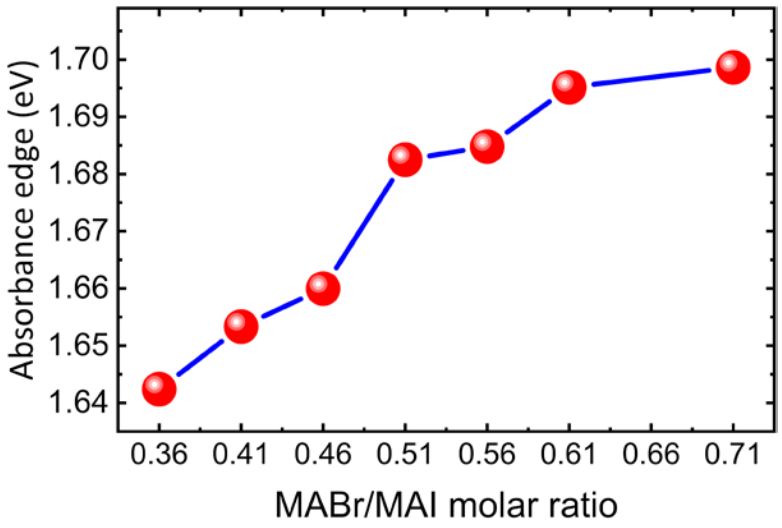

Figure S5. Evolution of the absorbance edge versus the MABr/MAI molar ratio

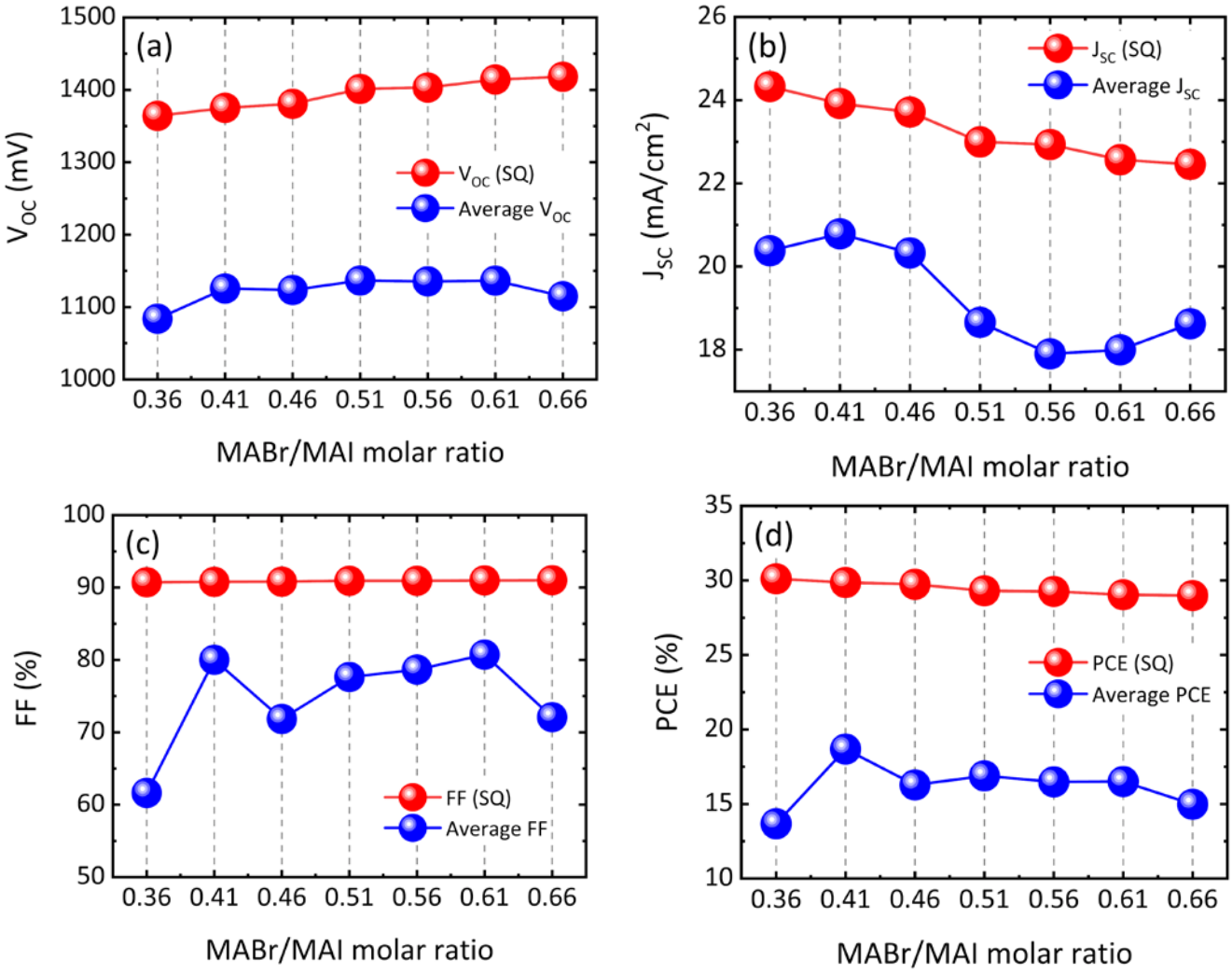

Figure S6. Shockley-Queisser limit and average values of V_{OC} (a), J_{SC} (b), FF (c) and PCE (d) for various MABr/MAI ratios.

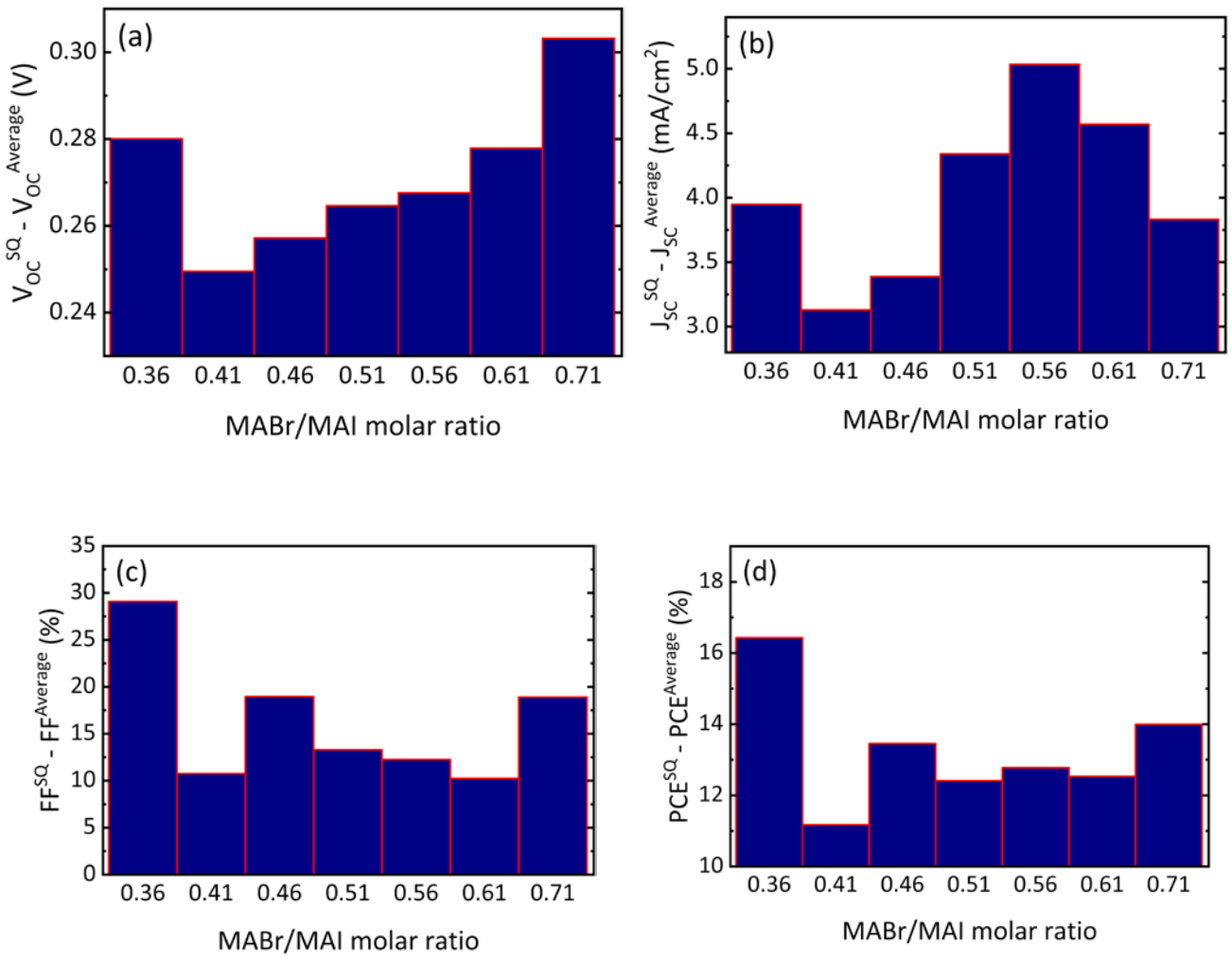

Figure S7. The calculated difference between the average measured V_{OC} (a), J_{SC} (b), FF (c) and PCE (d) with the values defined by the Shockley- Queisser limit measured for the samples prepared from different MABr/MAI ratios.

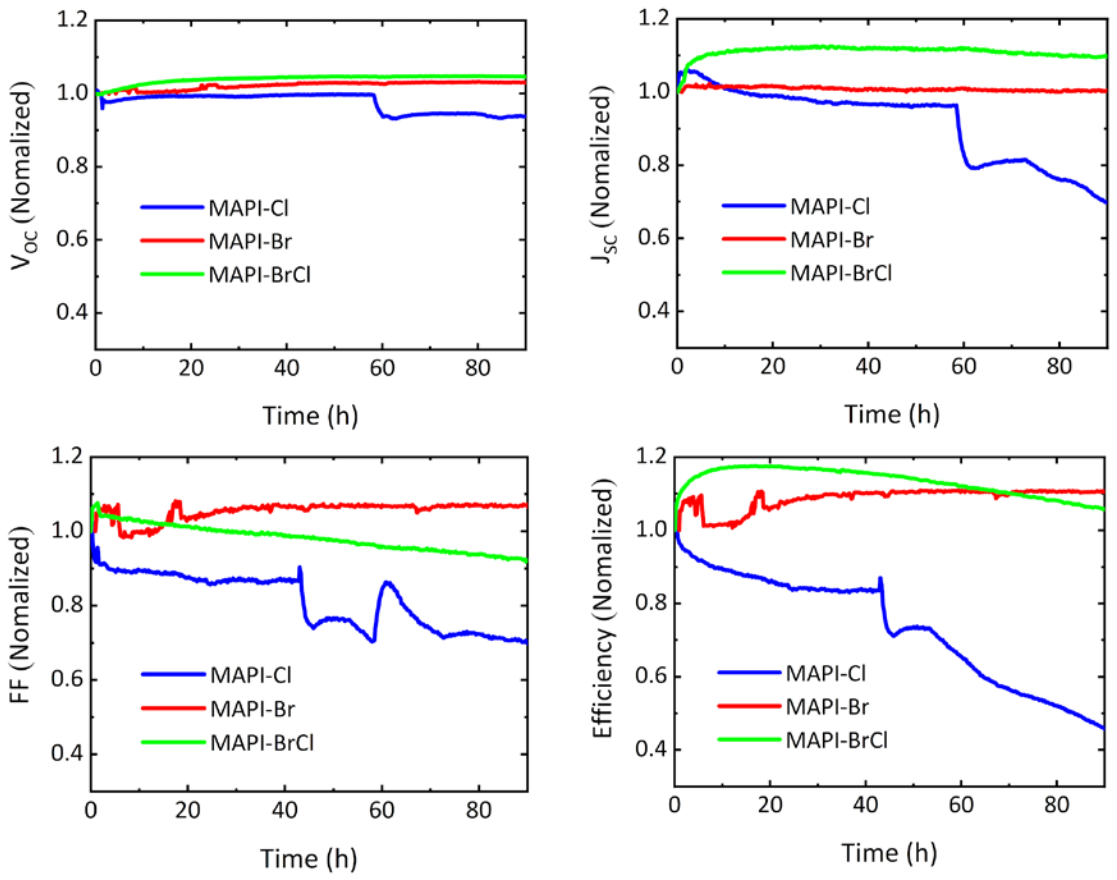

Figure S8. Stability analysis for MAPI, MAPI-Cl, MAPI-Br, and MAPI-BrCl based on IV measurements taken every 15 minutes under continuous one sun irradiance.

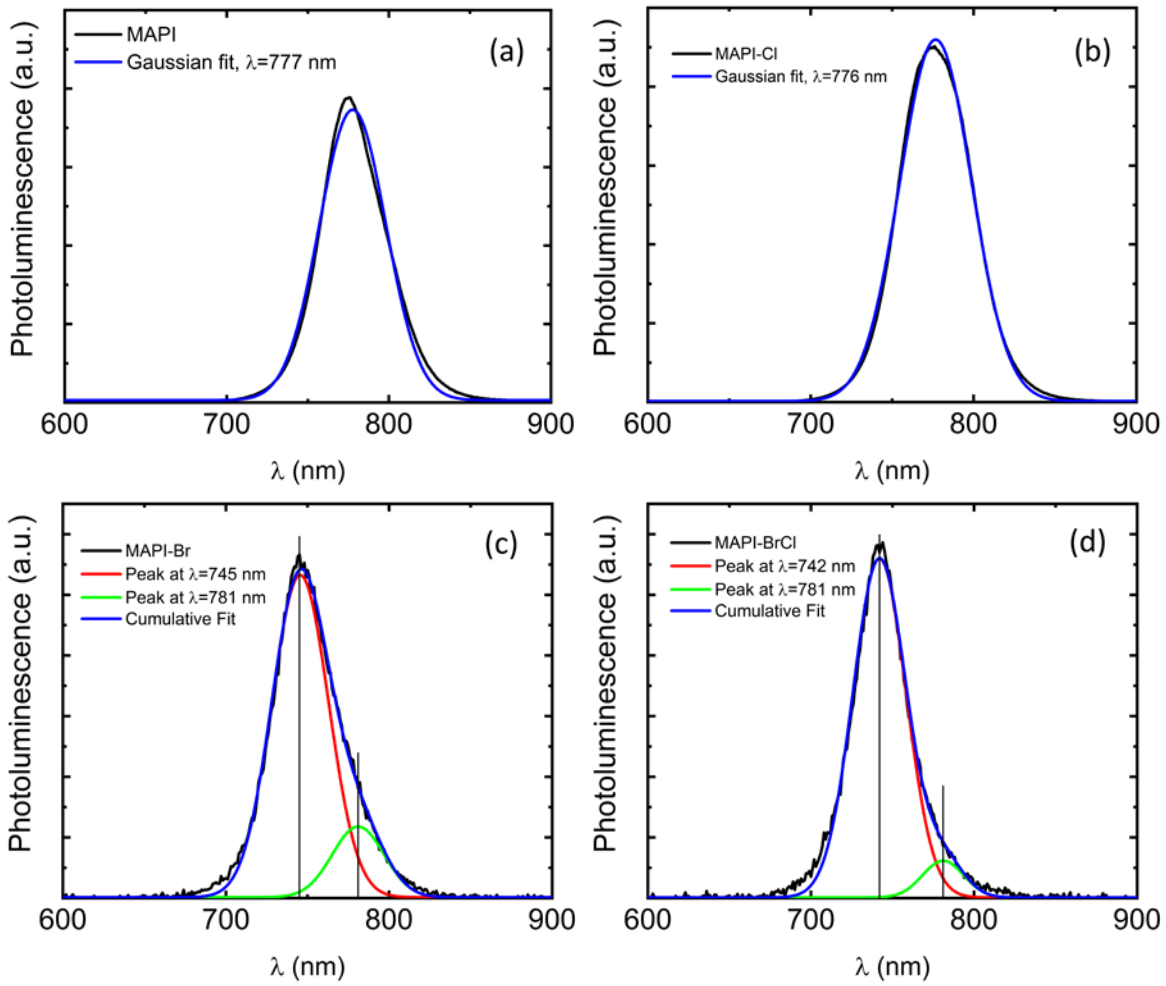

Figure S9. (a), (b), (c), and (d) respectively depict the photoluminescence spectra of MAPI, MAPI-Cl, MAPI-Br, and MAPI-BrCl. Gaussian fit has been used to as the fitting method.